Strong–field induced fragmentation and isomerization of toluene probed by ultrafast femtosecond electron diffraction and mass spectrometry

Journal:	*Faraday Discussions*
Manuscript ID	FD-ART-11-2020-000125.R1
Article Type:	Paper
Date Submitted by the Author:	11-Dec-2020
Complete List of Authors:	Xiong, Yanwei; University of Nebraska - Lincoln Borne, Kurtis; Kansas State University Carrascosa, Andrés; Brown University Kumar Saha, Sajib; University of Nebraska - Lincoln Wilkin, Kyle; University of Nebraska - Lincoln Yang, Mengqi; Louisiana State University, Chemistry Bhattacharyya, Surjendu; Kansas State University Chen, Keyu; Kansas State University Du, Wenpeng; Brown University Ma, Lingyu; Brown University Marshall, Nathan; Kansas State University F. Nunes, J. Pedro; University of Nebraska-Lincoln Pathak, Shashank; Kansas State University Phelps, Zane; Kansas State University Xu, Xuan; Brown University Yong, Haiwang; Brown University, Lopata, Kenneth; Louisiana State University, Weber, Peter; Brown University, Dept. of Chemistry Rudenko, Artem; J. R. Macdonald Laboratory, Rolles, Daniel; Kansas State University, Physics Centurion, Martin; University of Nebraska - Lincoln,

Strong-field induced fragmentation and isomerization of toluene probed by ultrafast femtosecond electron diffraction and mass spectrometry

Yanwei Xiong[1], Kurtis Borne[2], Andrés Moreno Carrascosa[3], Sajib Kumar Saha[1], Kyle J. Wilkin[1], Mengqi Yang[4] ,Surjendu Bhattacharyya[2] , Keyu Chen[2], Wenpeng Du[3], Lingyu Ma[3] , Nathan Marshall[2] , J. Pedro F. Nunes[1], Shashank Pathak[2], Zane Phelps[2], Xuan Xu[3], Haiwang Yong[3], Kenneth Lopata[4], Peter M. Weber[3], Artem Rudenko[2], Daniel Rolles[2], Martin Centurion[1]

[1]*University of Nebraska – Lincoln, Lincoln Nebraska, USA*

[2]*Kansas State University – Manhattan, Kansas, USA*

[3]*Brown University - Providence, Rhode Island, USA*

[4]*Louisiana State University, Baton Rouge, Louisiana, USA*

We investigate the fragmentation and isomerization of toluene molecules induced by strong-field ionization with a femtosecond near-infrared laser pulse. Momentum-resolved coincidence time-of-flight ion mass spectrometry is used to determine the relative yield of different ionic products and fragmentation channels as a function of laser intensity. Ultrafast electron diffraction is used to capture the structure of the ions formed on a picosecond time scale by comparing the diffraction signal with theoretical predictions. Through the combination of the two measurements and theory, we are able to determine the main fragmentation channels and to distinguish between ions with identical mass but different structures. In addition, our diffraction measurements show that the independent atom model, which is widely used to analyze electron diffraction patterns, is not a good approximation for diffraction from ions. We show that the diffraction data is in very good agreement with *ab-initio* scattering calculations.

1. Introduction

The ionization of toluene, C_7H_8, produces multiple fragments and triggers several rearrangement reactions, including the formation of the symmetric 7-ring tropylium cation and the sigmatropic shifts of hydrogen atoms[1-4] (see Figure 1). The toluene system has been studied using mass spectroscopy, including investigations of the isomerization pathway of $C_7H_7^+$[1-7]. The cation yield when ionizing in intense laser fields depends on the laser intensity[8-11] and the wavelength[12]. Mass spectrometry experiments can identify the different fragments by mass, but cannot alone differentiate between isomers. For this reason, mass spectra are often combined with other measurements to determine isomer ratios, e.g. by using Coulomb explosion imaging[13]. Gas electron diffraction has a long history in the determination of the structure of neutral molecules[14] and has recently been coupled with synchronous mass spectrometry[15, 16]. Ultrafast electron diffraction (UED) has been a valuable tool to capture molecular structures on the picosecond scale[17-19] and more recently to trace nuclear wavepacket dynamics on femtosecond time scales[20-26]. Electron diffraction has also been used to study the structure of cluster ions by scattering an electron beam from ions captured in a Paul trap [27-30], but as far as we are aware, there have not been any UED studies of ionized molecules in the gas phase. There are challenges in gas-phase UED from ions that are not present for neutral molecules. The first is that ionization in the gas creates a plasma that can distort the incoming electron beam[31]. The second is that the independent atom model (IAM), which is commonly applied to analyze and interpret UED data, is not a good approximation for scattering from ions. The IAM

1

assumes that the total scattering is the sum of the scattering from the individual atoms that make up a neutral molecule, ignoring bonding electrons and any net charge. Corrections to the IAM model have been considered to include bonding effects to more accurately determine the structure of neutral molecules[32]. In the case of ions, there is no straightforward way to correct for the net charge, which may be distributed across the molecule, thus an *ab initio* scattering calculation is preferable.

Here we present a multimodal investigation of the strong-field induced ionization, isomerization and fragmentation of toluene. The toluene molecules are ionized with a femtosecond laser pulse, and the ionic products are measured using momentum-resolved coincidence ion time-of-flight mass spectrometry (TOF-MS) and gas-phase UED. The momentum-resolved TOF-MS measurement determined the mass-to-charge ratio, momentum, and yield of each ion produced by the interaction with the laser pulse. In the UED measurement, a femtosecond electron pulse is scattered from the molecules a few picoseconds after the ionization. The UED signal is composed of the sum of the scattering from ionized and neutral molecules in the interaction volume. While TOF-MS can separate the ions by mass, it is not directly sensitive to structure. Specifically, it cannot distinguish between the $C_7H_7^+$ isomers tropylium and benzyl (see Figure 1). For the case when a single structure is present, the diffraction pattern can be directly compared with a model of the structure to determine the nuclear geometry. However, unambiguous structure determination is generally not possible if many unknown structures are present. We therefore use the results of the TOF-MS measurement to determine the most prevalent fragments and limit the number of structures in the UED data analysis. We then perform Complete Active Space Self Consistent Field (CASSCF) calculations to model the most likely structure of each fragment, and use an *ab-initio* scattering calculations to derive simulated UED signals for each fragment. The best fit between experiment and theory is found by comparing the measured signal to a simulated scattering signal where the abundance of each fragment is parameterized. From the results, we can determine the yield of different fragments, including isomers. This work establishes a method to combine TOF-MS and UED data, and shows that UED experiments from ions cannot be accurately modeled with the IAM but are in good agreement with *ab-initio* scattering calculations. In this work, we have used UED to capture the molecular structures on picosecond time scales, however, the methods demonstrated here can also be applied in UED experiments with femtosecond resolution[21, 22, 26] to capture the structural dynamics that lead to fragmentation in ionized molecules.

2. Experiment setup
2.1 Ultrafast electron diffraction

The UED setup comprises a DC photoelectron gun, electron beam optics, an RF cavity to compress the electron pulses, a target chamber, the detector and the synchronization electronics, all of which were described in detail in previous publications [33, 34]. A femtosecond laser with pulse duration of 50 fs, 2 mJ energy and 5 kHz repetition rate is used to trigger electron emission from the photocathode and to ionize the molecules. The molecules are ionized with the fundamental wavelength of the laser at 800 nm, while a frequency tripler is used to trigger the photoemission with a wavelength of 267 nm. Figure 2 shows the layout of the experimental setup including the laser system, the electron beamline, the RF synchronization and compression, and the interaction region. The laser system consists of a mode locked oscillator and a Ti: sapphire amplifier. The electron beamline comprises a cathode, a DC electric field that accelerates the electron pulse to a kinetic energy of 90 keV, magnetic deflectors, and a magnetic lens. The RF compression cavity has a 3 GHz longitudinal electric field that changes the velocity distribution of the electron pulses

such that it compresses longitudinally with a minimum pulse duration at the sample. The RF field in the cavity is timed using a home-made system that synchronizes the RF field to the 75 MHz repetition rate of the laser oscillator, following an earlier design [35]. A small fraction of the seed laser power, with repetition rate of 75 MHz, triggers a fast photo-diode to generate an electronic signal. This signal is filtered to select the 40th harmonic at 3GHz, which is then amplified via multiple low phase noise amplifiers and a high power amplifier to drive the RF cavity. A phase shifter is used to select the optimal phase of the RF cavity for compression by measuring the electron pulse duration using a streak camera[36]. A feedback loop is used to correct phase noise introduced by the high power amplifier. The system has been characterized over several hours to have a timing jitter of 50 fs rms.

In the interaction region (see the inset in Figure 2), toluene molecules are introduced seeded in a helium beam through a 50 μm nozzle. The total backing pressure on the nozzle is 140 torr, with a mix of 6 to 1 of helium to toluene. The diameter of the gas jet at the interaction region is 350 μm FWHM. A platinum aperture, 15 mm away at the upstream of the nozzle, is used to reduce the electron beam size to 100 μm FWHM. The number of electrons on the sample is 8,800 per pulse, corresponding to 7 pA of beam current. The scattered electrons are recorded using a phosphor screen optically imaged onto an electron-multiplying charge-coupled device (EMCCD). The directly transmitted electron beam is stopped using a beam block positioned in front of the screen to prevent saturation of the images. The spatial and temporal overlap of the laser and electron pulses is determined using the plasma lensing effect, where the laser is tightly focused to produce a strong plasma that distorts the electron beam [31]. The ionizing laser pulse has a time duration of 50 fs (FWHM), energy of 1.2 mJ and is focused to a spot size of 100 μm (H)× 170 μm (V) FWHM on the sample. The peak laser intensity on the sample is 116 ± 20 TW/cm^2. The value of the peak intensity is based on the measurements of laser pulse energy, duration and the spot size, and assumes a Gaussian temporal profile. The uncertainty in the intensity reflects the uncertainty in the measurement of the spot size. The angle between the laser and electron beam is 60 degrees. The overall temporal resolution of experiment is estimated to be 600 fs. The resolution is limited by the temporal broadening due to the velocity mismatch between laser and electron pulses, [37], which can in principle be improved using laser pulses with a tilted wavefront [26].

2.2 Momentum-resolved coincidence ion time-of-flight mass spectroscopy

In order to determine the ionic products that are generated upon strong-field ionization of gaseous toluene as a function of (peak) intensity, a complementary momentum-resolved coincidence ion time-of-flight mass-spectroscopy experiment was conducted within the same intensity regime as used in the UED experiment. The experimental setup was similar to the one described in Ref. [38] but without splitting the laser beam into pump and probe pulses. Briefly, the linearly polarized output of a 2 mJ, 10 kHz Ti: Sapphire laser with a central wavelength of 794 nm was attenuated and focused on a gaseous molecular sample via a 75 mm back-reflecting spherical mirror that produced a focal spot diameter ($1/e^2$) of approximately 3 μm (calculated from the size of the incident beam by assuming a perfect Gaussian beam) centered on the molecular beam. The laser pulse duration during the experiment was 29 fs, as determined from a frequency-resolved optical gating (FROG) measurement. Peak intensities ranging from 30 to 220 TW/cm^2 were chosen to cover the intensity range sampled by UED experiment. The peak intensity in the interaction region for the TOF-MS measurement was calibrated using change of the slope corresponding to the onset of rescattering plateau in the recoil momentum spectrum of the Ne$^+$ ion [39, 40] at 407 ± 54 TW/cm^2 and scaling this value according to the pulse energy used for the TOF-MS data, which was controlled via a combination of half-wave plate and thin-film polarizer.

Gaseous toluene was introduced into the experimental chamber as a supersonic molecular beam mixed with 250 Torr of helium as a carrier gas. The continuous molecular beam was introduced through a 30 μm flat nozzle and collimated by a series of skimmers and apertures that separated the expansion chamber from the interaction chamber, which had a base pressure of approximately 5×10^{-11} Torr. At the position where it was crossed by the laser beam at an angle of 90°, the molecular beam had a diameter of approximately 4 mm (estimated geometrically from the arrangement of the skimmers and apertures that confined the beam). Ions generated by the interaction of the toluene beam with the laser pulses were detected using a COLTRIMS-type [41, 42] ion momentum imaging spectrometer with a uniform electric field (field strength 126 V/cm) parallel to the laser polarization. Under these conditions, all ions with the kinetic energies up to 17 eV emitted in the full 4π solid angle were guided to a time- and position-sensitive delay-line anode microchannel plate (MCP) detector The amplified MCP and delay-line signals for each detected ion were processed by a constant fraction discriminator (CFD) and a multi-hit time-to-digital converter, and recorded shot-by-shot in a list-mode event file. The detector was operated with 2950 V bias voltage at the front plate, which, together with the selected CFD settings, ensured an approximately uniform detection efficiency for all ions independent of their mass-to-charge ratio[43]. From the time-of-flight and detector hit positions, the mass-to-charge ratio and three-dimensional momentum vector of each ion was determined assuming classical motion in the homogeneous electric field of the spectrometer.

3. Theory

3.1 Electron scattering calculation with independent atom model

The elastic scattering from a neutral molecule can be approximated using the diffraction theory based on the independent atom model (IAM). The diffraction intensity is an incoherent sum of scattering from individual molecules, in which electron waves scattered from atoms within a molecule interfere. Within the IAM, the diffraction signal of one molecule is written as $I(s) = \left|\Sigma_{n=1}^{N\_atoms} f_n(s)\exp\left(-i\vec{s}\cdot\vec{r_n}\right)\right|^2$, where N_{atoms} is the total number of atoms in the molecule, $\vec{s}$ is the momentum change with magnitude $s = \frac{4\pi}{\lambda}\sin\left(\frac{\theta}{2}\right)$, θ is the scattering angle, λ is the deBroglie wavelength and $\vec{r_n}$ is the location of the nth atom. The diffraction intensity of a randomly oriented molecular ensemble is calculated by averaging over all possible orientations of the molecules, which can be separated into the atomic scattering term I_{at} and molecular scattering term I_{mol}.

$$I_{total} = I_{at} + I_{mol} \tag{1a}$$

$$I_{at} = \Sigma_{n=1}^{N_{atoms}}|f_n(s)|^2 \tag{1b}$$

$$I_{mol} = \Sigma_{i=1}^{N_{atoms}}\Sigma_{j\neq i}^{N_{atoms}}|f_i(s)||f_j(s)|\cos\left[\eta_i(s)-\eta_j(s)\right]\frac{\sin(sr_{ij})}{sr_{ij}} \tag{1c}$$

$$sM = \frac{sI_{mol}}{I_{at}} \tag{1d}$$

where $|f_i(s)|$ and $\eta_i(s)$ are the magnitude and phase of the form factor of the ith atom, and r_{ij} is the distance between i^{th} and j^{th} atom. The structural information of the molecule is encoded in I_{mol}. The modified diffraction pattern sM is defined by equation (1d). A common way to investigate the change of molecular structural information is to calculate the diffraction difference intensity $\Delta I_{mol}(s,t) = I_{total}(s,t)-I_{total}(s,t_{ref})$ [44]. Here $I_{total}(s,t)$ is the scattering intensity measured at time t after the laser excitation, and $I_{total}(s,t_{ref})$ is a reference diffraction pattern recorded with the electrons arriving at the sample before the laser to capture

the ground state signal, which is used to remove the atomic scattering intensity and experimental background.

Even though the IAM is a reasonable approximation for the description of electron scattering from neutral molecules in their ground electronic states, the coherent sum of pretabulated atomic potentials is insufficient when the charge distribution within the molecule changes significantly upon excitation. In the case of photoionization in particular, IAM is unable to account for the placement of a charge within the molecule, necessitating a more detailed description of the electron density in order to calculate the scattering from ionized species.

3.2. Ab initio computation of electron scattering

To calculate the elastic electron scattering intensity beyond the independent atom model and provide a correct representation of the electronic charge distributions, one formulates the electron scattering signal in terms of the one-electron density of the molecule, $\rho(r)$, obtained from a direct treatment of the molecular electronic wavefunction and the geometry of the molecule. This method not only provides a better description of the electron diffraction process than IAM by appropriately distributing all molecular charges, it also enables a correct representation of the cationic products created in the toluene photo ionization and fragmentation. The rotationally averaged elastic electron scattering intensity within the first-Born approximation can be defined as,

$$s^4 I_{total}/I_{Ruth} = I_{ee}/I_{Th} + I_{ne} + I_{nn} \tag{2a}$$

where I_{total} is the elastic electron scattering signal, I_{Ruth} is the Rutherford cross-section and I_{Th} is the Thomson cross-section. For scattering from an ensemble of molecules without any degree of alignment a full rotational averaging of the signal is necessary as described above.

The three terms in Eq. (2a) express the different interactions between the electron and the molecule in the diffraction process. I_{ee} represents the electron-electron interaction and it is analogous to the elastic intensity in x-ray scattering,

$$I_{ee}(s) = \langle |\int \rho^{(N)}(r)\, e^{-\imath sr} dr|^2 \rangle_{\theta,\phi} \tag{2b}$$

where $I_{ee}(s)$ corresponds to the Fourier transformation of the one-electron density $\rho^{(N)}(r)$ for the N-electron system, r are the electronic coordinates and $\langle ... \rangle_{\theta,\phi}$ represents the rotational averaging of the signal.

The second term in Eq. (2a), I_{ne}, contains the nuclear-electron interactions of the scattered electron and it can be related to the Fourier transformation of the molecular one-electron density, $\rho^{(N)}(r)$,

$$I_{ne} = -2\sum_{i}^{N_{atoms}} Z_i \langle \int \rho^{(N)}(r)\, e^{\imath sr}\, dr\, e^{-\imath sR_i} \rangle_{\theta,\phi} \tag{2c}$$

where N_{atoms} is the number of atoms in the molecule, Z_i is the charge of the ith atom in the molecule and R_i is the ith atomic position. The last term in Eq. (2a) represents the nuclear-nuclear interaction and it only depends on the atomic positions R_i, and the atomic charges Z_i,

$$I_{nn} = \sum_i^{N_{atoms}} \sum_j^{N_{atoms}} Z_i Z_j \frac{sin\,(s|R_i - R_j|)}{s|R_i - R_j|}$$
(2d)

where the zeroth order spherical Bessel function, $\frac{sin\,(s|R_i - R_j|)}{s|R_i - R_j|}$, guarantees the full rotational averaging of the nuclear-nuclear term.

The analytical evaluation of Eqs. (2a-2d) using *ab-initio* molecular wavefunctions can be performed using the methods outlined in Ref. [45, 46]. This procedure overcomes the common problem encountered in the IAM treatment as it adequately describes the distortion of the electron density in molecules due to chemical bonding [47], it is also valid to describe electron diffraction from excited states and charged systems.

The modified diffraction pattern *sM(s)* still depends on the atomic contribution I_{atomic} to the total signal. The individual atomic form-factors can be reconstructed using the same wavefunction-based method and subtracted from I_{total} to build the *sM(s)*.

4. Results
4.1 Momentum-resolved ion time-of-flight mass spectra

We have measured the momentum-resolved ion TOF spectra of gas-phase toluene after strong-field ionization with 800-nm laser pulses at peak intensities between 30 and 220 TW/cm^2. As an example, the TOF spectrum for a peak intensity of 130 TW/cm^2 is shown in Figure 3. Strong contributions from the parent ion ($C_7H_8^+$), parent dication ($C_7H_8^{2+}$), and the parent ion with one hydrogen or proton loss ($C_7H_7^+$) are observed along with several broad peaks corresponding to singly charged $C_mH_n^+$ fragments (m = 1-6, n = 0-8). The width of the latter is mainly due to significant kinetic energy release resulting from molecular fragmentation. In the (non-coincident) TOF spectrum in Figure 3, we can thus only resolve the groups corresponding to different numbers of carbon atoms, *m*, but not the individual peaks corresponding to a different number of hydrogen atoms, *n*. The integrated yield of $C_7H_8^{2+}$, $C_7H_7^+$, and each $C_mH_n^+$ fragment group, normalized to the yield of the $C_7H_8^+$ parent ion, for different peak intensities is given in Table 1.

Further information on the kinetic energy of the detected ions can be gained when plotting a projection of the detector hit position as a function of the ion TOF, as shown in the bottom panel of Figure 3. For each mass-to charge ratio, this graphs represents a scaled 2D projection of the 3D momentum distribution of the corresponding ion. Ions detected near the center of the detector (*y*=0) and in the middle of the corresponding time of flight peak have very small kinetic energies and, thus, correspond to ionic fragments generated by dissociative single ionization. In most cases, they are produced along with one neutral fragment that carries the remaining mass. In contrast, fragment ions produced by the Coulomb explosion of a dication produced via double ionization of the toluene molecule (or by the higher charge states) carry significant kinetic energy and spread out in both the detector hit position and the time of flight, thus appearing as ring- or disk structures in the two dimensional spectrum. The relative contribution of fragments stemming from single and double (or multiple) ionization can therefore be estimated by integrating the ion yields from each $C_mH_n^+$ group within the regions of interest shown as white and black dashed rectangles, respectively, for the representative example of the $C_4H_n^+$ group. The corresponding yields are given in Tables 2 and 3. It is important to note that the separation into "low" and "high" kinetic energy ions solely based on the appearance in this two-dimensional spectrum is only an approximation since a precise determination of the

three-dimensional momentum and, thus, the kinetic energy is not possible for overlapping peaks of (non-coincident) ions with different mass-to-charge ratios. Nevertheless, inspection of the values in Table 2 and 3 shows that with the exception of $C_6H_n^+$ fragments produced at the lower end of the covered intensity range, the majority of $C_mH_n^+$ fragments have high kinetic energies and are therefore created from double (or multiple) ionization.

These findings are consistent with the analysis of a photoion-photoion coincidence spectrum, which is not shown here. Furthermore, this spectrum together with the two-dimensional TOF vs. position spectra allows us to identify the ion species that contribute most strongly to each of the $C_mH_n^+$ fragment groups, which we list in the following in parentheses for each group, with the strongest fragments for each group shown in bold font: $CH_n^+(CH_2^+, \mathbf{CH_3^+})$, $C_2H_n^+(\mathbf{C_2H_2^+, C_2H_3^+})$, $C_3H_n^+(\mathbf{C_3H_3^+}, C_3H_4^+, C_3H_5^+)$, $C_4H_n^+(\mathbf{C_4H_3^+, C_4H_4^+}, C_4H_5^+)$, $C_5H_n^+(\mathbf{C_5H_3^+, C_5H_5^+}, C_5H_6^+)$, $C_6H_n^+(\mathbf{C_6H_5^+, C_6H_6^+})$. This information allows us to limit the selection of ions and fragment pairs used to fit the UED data, as explained in the following.

Table 1. Abundance of different fragment ions normalized to the yield of the $C_7H_8^+$ parent ion. Note that the time scale of the TOF-MS measurements is on the order of several microseconds (see Figure 3).

I (TW/cm^2)	CH_n^+	$C_2H_n^+$	$C_3H_n^+$	$C_4H_n^+$	$C_5H_n^+$	$C_6H_n^+$	$C_7H_8^{2+}$	$C_7H_7^+$
220	17.1%	26.3%	30.9%	17.6%	17.2%	2.3%	4.8%	16.0%
170	8.6%	17.2%	21.0%	12.9%	13.9%	1.8%	3.5%	15.8%
130	4.7%	11.2%	13.9%	9.1%	10.9%	1.4%	2.5%	15.1%
90	1.2%	3.7%	5.0%	3.7%	5.7%	0.6%	1.1%	12.3%
65	0.5%	1.6%	2.4%	1.9%	3.4%	0.4%	0.6%	10.0%
30	0.4%	0.5%	0.8%	0.7%	1.3%	0.1%	0.1%	6.3%

Table 2. Abundance of fragments with high kinetic energies, normalized to the yield of the $C_7H_8^+$ parent ion.

I (TW/cm^2)	CH_n^+(high)	$C_2H_n^+$(high)	$C_3H_n^+$(high)	$C_4H_n^+$(high)	$C_5H_n^+$(high)	$C_6H_n^+$ (high)
220	14.2%	20.2%	22.3%	12.9%	10.5%	0.6%
170	7.0%	13.6%	15.4%	9.2%	8.0%	0.5%
130	3.8%	8.9%	10.2%	6.4%	5.8%	0.4%
90	1.0%	2.9%	3.6%	2.5%	2.4%	0.2%
65	0.4%	1.2%	1.6%	1.2%	1.2%	0.1%
30	0.4%	0.3%	0.5%	0.4%	0.4%	0.0%

Table 3. Abundance of fragments with low kinetic energies, normalized to the yield of the $C_7H_8^+$ parent ion.

I (TW/cm^2)	CH_n^+(low)	$C_2H_n^+$(low)	$C_3H_n^+$(low)	$C_4H_n^+$(low)	$C_5H_n^+$(low)	$C_6H_n^+$(low)
220	2.9%	6.1%	8.6%	4.7%	6.7%	1.7%
170	1.6%	3.6%	5.6%	3.6%	5.9%	1.3%

130	0.9%	2.3%	3.7%	2.7%	5.1%	1.0%
90	0.2%	0.8%	1.5%	1.3%	3.3%	0.4%
65	0.0%	0.4%	0.8%	0.7%	2.2%	0.3%
30	0.0%	0.3%	0.3%	0.3%	0.9%	0.1%

4.2 ΔsM simulation

In order to simulate the UED signal, the fragmentation products are assumed to be the same as those measured in the TOF-MS experiment (listed in table 1). We have calculated the ground-state geometry of the neutral and ionic fragments of using a Complete Active Space Self Consistent Field (CASSCF) level of theory and 6-311G basis sets using the electronic structure package Molpro [48]. The multiconfigurational character of this method correctly accounts for static electron correlation in the ground electronic state and increases the accuracy in the ground state geometry optimization in respect to other single reference methods. The active spaces and electrons considered for each fragment are listed in Table 4. They have been chosen to allow an accurate multideterminant description of the wavefunction and assure a compromise between accuracy and computational time. The electron scattering signals are simulated using the analytical method presented in the theory section 3.2 and outlined in previous publications[45, 47].

Table 4. CASSCF level of theory for the geometry optimization and electron scattering signal calculation. Each of the fragments is considered in its cationic and neutral form. The multiplicity of the fragments is changed accordingly. m is the number of active orbitals and n the number of active electrons.

Fragments	CH_3^+	CH_3	CH_2^+	CH_2	$C_2H_3^+$	C_2H_3	$C_2H_2^+$	C_2H_2	$C_3H_4^+$	$C_3H_5^+$
(m, n)	8,6	8,7	7,7	7,8	10,11	10,12	10,9	10,10	12,17	12,18
$C_3H_3^+$	$C_3H_2^+$	C_3H_3	C_3H_4	C_3H_5	C_3H_2	$C_4H_3^+$	C_4H_4	$C_4H_4^+$	$C_4H_5^+$	C_4H_5
12,16	10,17	12,17	12,18	12,19	10,18	8,10	8,12	8,11	8,12	8,13
C_4H_3	$C_5H_6^+$	C_5H_3	C_5H_6	$C_5H_3^+$	C_5H_5	$C_5H_5^+$	$C_6H_6^+$	C_6H_3	C_6H_6	$C_6H_3^+$
8,10	11,15	11,13	11,16	11,12	11,15	10,14	9,11	9,9	9,12	9,8
$C_6H_5^+$	C_6H_5	Bz^+	CHT^+	Tr^+	Tol^+	Tol^{2+}	Tol	H		
8,10	9,11	8,9	8,9	8,8	8,9	8,8	8,10	3,1		

In order to simulate the scattering signal, we assume that each fragmentation event of a toluene molecule produces only two fragments, called fragment pairs in the following text. This assumption neglects breakup into more than two fragments, which we assume to be a minor contribution at the given laser intensities. Furthermore, in accordance with the observations from the momentum-resolved ion imaging experiment, we explicitly consider the cases where one of the fragments in the pairs is charged and the other one neutral, i.e. dissociation after single ionization, and those cases where both fragments are charged, corresponding to double ionization and subsequent Coulomb explosion. The simulated diffraction difference signal for a

certain fragment pair, i.e. C_6H_5, CH_3^+, is calculated as $\Delta I(s) = I_{C_6H_5}(s) + I_{CH_3^+}(s) - I_{toluene}(s)$, and for benzylum (Bz$^+$ $C_7H_7^+$), $\Delta I(s) = I_{Bz^+}(s) + I_H(s) - I_{toluene}(s)$. The corresponding modified diffraction signal is $\Delta sM(s) = s\Delta I(s)/I_{atom\_toluene}$, where $I_{atom\_toluene}$ is the atomic scattering intensity of the neutral toluene molecule.

The *ab initio* calculation of elastic electron scattering for fragment pairs are shown in Figure 4 using the sM(s) convention. The sM of tropylium (Tr$^+$) is close to that of cycloheptatriene (CHT$^+$), and the sM of the toluene cation (Tol$^+$) is close to 1/3 times the sM of Tol^{2+}. Figure 4 shows that the sM of fragment pairs can be classified to 6 groups, (C_3H_m, C_4H_n), (C_6H_m, CH_n), (C_2H_m, C_5H_n), (Tr^+, CHT^+), (Tol^+, Tol^{2+}), and Bz$^+$. The elastic electron scattering simulation for the abovementioned fragment pairs utilizing the independent atomic model are shown in section S4 of the supplemental material for comparison. The most prominent cations from each group measured from time-of-flight mass spectroscopy are used for the fitting of the UED data, as explained in the following section.

4.3 Ultrafast electron diffraction measurements

We recorded a static diffraction pattern of toluene, and then recorded diffraction at different relative delays between the 800-nm pump laser pulse and the electron pulse. Figure 5 shows the data from the static diffraction pattern. The two-dimensional static diffraction patterns from toluene molecules are azimuthally averaged to obtain 1-dimensional $I_{total}(s)$. Equations (1a-1d) are used to calculate the modified diffraction intensity sM(s) for the static diffraction signal. The zero values of the calculated sM are used to fit and remove a background from the experimental $I_{total}(s)$. [44]. The removed background is composed of the atomic scattering, other experimental background scattering and noise. The background removal gives the $I_{mol}(s)$, shown in figure 5(a), from which the sM shown in Figure 5(b) is calculated. There is good agreement between the measured and theoretical sM.

Pump-probe diffraction patterns were acquired at four different relative delays between laser and electron pulses: -5 ps, 5 ps, 10 ps and 15 ps. The data at negative delay times corresponds to electrons arriving at the sample before the laser pulse. This data contains scattering from ground state toluene molecules and other background signals such as scattered laser light and background electrons, and will be used as a reference. Data was acquired for a total of 100 minutes at each time delay. Figure 6 shows the ΔsM signal at each time delay, where $\Delta sM(s,t) = s\dfrac{I_{total}(s,t) - I_{total}(s,t_{ref})}{I_{at}}$, and $I_{total}(s,t_{ref})$ is the data recorded at t = -5 ps. The signal shows larger statistical variations at larger s, which are due to the lower signal level. We did not see significant differences at the different delay times, which suggest that there is no further fragmentation on the picosecond time scale, although there could be some fragmentation on longer time scales.

As described above, we used simulated ΔsM from the most prevalent fragments, as determined from TOF-MS, to fit the experimental data. Fitting to the individual time steps gave consistent results within the experimental uncertainties, so we show here fitting to the combined data set (average of all time steps) to reduce uncertainties. The fragments used for the fitting were: $(C_4H_4^+, C_3H_4^+)$, $(C_6H_5^+, CH_3^+)$, $(C_5H_3^+, C_2H_3^+)$, Tr$^+$, Bz$^+$ and Tol$^+$. All fragments were assumed to have a charged partner, based on the momentum-resolved TOF-MS measurements that showed that the majority of the fragments are produced by double ionization. The fit results did not change significantly by including a small fraction of neutrals. Figure 1 shows three-dimensional models of the fragments based on the calculated structures. The fragments in parenthesis are fragment pairs formed during the breakup of the parent molecule.

We note that in order to simplify the calculations, the geometry optimization was performed for fragments in their respective electronic ground states even though some fragments might be produced in electronically and/or vibrationally excited states. Accurate simulation of excited state patterns of each fragment can be challenging and is beyond the scope of this work. We expect that most fragments, many of which are open-shell systems, would have returned to the electronic ground state after 5 ps. It has also been demonstrated before in the case of x-ray scattering experiments that the electronic excitation manifests as a secondary contribution to the scattering signal and is approximately an order of magnitude smaller than the effect of molecular geometry changes[49-51]. Therefore, the inclusion of vertically excited fragments is not likely to produce significant differences in the fitting procedure.

In addition, no corrections relating to vibrational excitation of the fragments have been applied to the signal. Very little is known about the internal energy with which fragments are borne in the photoionization process, so that at the present time inclusion of vibrational effects is not possible. Separate studies have shown that the effect from vibrational excitation, at least for rigid molecules, is small even at very high temperatures[51, 52].

The details of data analysis, fitting method and fitted parameters for the diffraction signal at different time delays are described in section S2 of the supplemental material. We used a bootstrapping algorithm to determine the confidence interval of the fitted parameters. Table 5 shows the result of the least-squares fit using the combined data. The analysis gives an excitation fraction of 12% (denoted as "ef" in the table) which corresponds to the fraction of molecules within the interaction volume that are ionized by the laser. The most prevalent structure in the fit is the parent ion, as expected. In our analysis, we included also the doubly ionized parent, since the structures are very similar and could not be separated by the diffraction measurement. Based on the TOF-MS measurements, we expect the singly ionized parent to be more prevalent. The fragment pair with the highest yield is C_5H_m,C_2H_n, followed by C_4H_m,C_3H_n and C_6H_m,CH_n. We have also detected a significant amount of Benzyl+. The tropylium and CHT cations have very similar structures, so that their abundance could not be determined independently, but we have observed a small but significant amount of Tr^+/CHT^+.

Table 5. Fitted abundance of products and χ^2 of the experimental ΔsM from combined data at 3 different time delays after time zero; "ef" denotes the total excitation fraction (see text)

Pairs	C_4H_m,C_3H_n	C_6H_m,CH_n	C_5H_m,C_2H_n	Tr^+, CHT^+	Bz^+	Tol^+,Tol^{2+}	ef	χ^2
%	7.30±1.71	5.40±1.82	13.14±2.01	2.66±1.15	5.31±4.68	66.20±4.44	0.12	1.88±0.08

5. Discussion
5.1 Comparison of UED and TOF-MS measurements

In this section, we compare the fragment yields as measured by TOF-MS and UED. While we aimed to make the measurements as comparable as possible, there are some significant differences. The first is the time scale. The TOF mass spectra are recorded when the ions reach the detector, i.e. microseconds after the ionization, while the UED data are captured within 5-15 ps after ionization. This leaves open the possibility that there will be further fragmentation between the time of ionization and when the TOF-MS data is captured. The second important difference is the intensity distribution. In the TOF-MS measurement, ions are collected from the whole focal volume defined by the intersection of the laser beam with the molecular

beam. In the UED data, the electron beam is smaller than the laser beam, so in this data, the higher intensity region of the focus is sampled more heavily as compared to the TOF-MS measurement. A more detailed analysis of this effect is given in the supplemental material. Furthermore, we note that the pulse durations of the 800-nm laser pulses that induced the fragmentation where not identical (30 fs for tTOF-MS and 50 fs for UED), which may lead to some differences in the branching ratios.

Another important technical difference is that TOF-MS is not sensitive to neutral fragments, while UED is sensitive to all fragments. In order to compare the two datasets, we therefore assume that for singly ionized fragments detected in the TOF-MS data, there is a complementary fragment that is neutral. For example, the yield of the neutral fragment C_3H_m is equal that of the $C_4H_n^+$ fragment in table 3. For the case of double ionization (high energy fragments in the TOF spectra), assuming the molecule breaks into two fragments, then both will be captured by the TOF-MS data. Thus, to calculate the total yield for a fragment pair including neutrals, we take the sum of the complementary pairs in the singly ionized data (Table 3) plus the yield of one of the complementary fragments measured in double ionization (Table 2). Assuming a two-body breakup, the two complementary fragments should show the same yield in double ionization, but we have observed some differences, most likely due to three-body fragmentation events that we have neglected here or due to some remaining dependence of the detection efficiency on the ions' mass, which have have tried to minimize but cannot exclude. Thus, to account for this uncertainty, we take as the lower bound the sum including the fragment with the lower yield and as a higher bound the fragment with the higher yield. For example, for the complementary pair (C_4H_m, C_3H_n), the lower bound is given by $C_4H_m^+(SI) + C_3H_n^+(SI) + C_4H_m^+(DI)$, where (SI) and (DI) indicates fragments produced by single and double ionization, respectively. The corresponding upper bound is given by $C_4H_m^+(SI) + C_3H_n^+(SI) + C_3H_m^+(DI)$.

Table 6 displays the relative fragment pair yields, calculated from the TOF-MS data to include both neutral and charged fragments, which can then be compared with the UED measurement. Table 7 shows the equivalent yields, normalized with respect to the yield of the parent ion, as calculated from the UED data. Based on this analysis, we see that the fragment yield of the UED experiment best matches the TOF-MS yield measured in the intensity range between 130 TW/cm² and 170 TW/cm². The UED experiment was carried out with a laser intensity of 116±20 TW/cm², but due to the different sampling of the intensity distribution as described above, it is expected that the yield would best match the TOF-MS data at a higher intensity. Overall, the results of the two measurement are consistent. A possible source of discrepancy is the different laser focusing geometry and the volume over which the fragments are sampled in the two experiments. Our *ab-initio* scattering calculations and the resulting fit to the experimental data assumed ionic fragments in their electronic and vibrational ground states and thus ignored other possible fragment geometries that may contribute to the diffraction signal. Three-body fragmentation could in principle play a role, however, our momentum-resolved ion-ion coincidence measurements suggest that this is only a minor fragmentation pathway.

Table 6. Relative yield of fragment pairs normalized to yield of $C_7H_8^+$ from TOF-MS. The two values in each column represent the lower and upper bounds for the yield of that fragment pair (see text).

I (TW/cm^2)	C_4H_m, C_3H_n	C_6H_m, CH_n	C_5H_m, C_2H_n
170	18.86% ~24.56%	3.44%~9.95%	17.44%~23.15%

130	12.98%~16.51%	2.30%~5.68%	13.19%~16.29%
90	5.15%~6.30%	0.78%~1.62%	6.54%~6.98%

Table 7. Relative yield of fragment pairs normalized to $C_7H_8^+$ from UED measurement.

Pairs	C_4H_m, C_3H_n	C_6H_m, CH_n	C_5H_m, C_2H_n
Abundance(%)	11.03±2.69	8.16±2.80	19.85±3.32

5.2 Comparison *Ab-initio* and IAM scattering calculations

We present a comparison of the data with *ab-initio* scattering calculations and with a calculation based on the IAM. A previous UED experiment on photo-excited pyridine has shown that the IAM does not accurately represent the diffraction signal at low s for times within 1.5 ps after excitation[53]. There was an enhancement of the diffraction signal at low s that was attributed to increased inelastic scattering from molecules in the excited state, and the total diffraction signal was well matched using high-level simulation of the excited state dynamics and *ab-initio* scattering calculations. Here we show that the IAM does not reproduce the diffraction signal for ions and that *ab-initio* scattering can reproduce the signal accurately. The largest difference between the two is present at small s, where the scattering from ions approaches Rutherford scattering.

In addition to the differences in elastic scattering from neutrals and ions, the UED signal at small angles can be distorted by the formation of a laser-induced plasma[31]. In a laser-induced plasma, electrons are separated from the positively charged parent ions. This separation creates macroscopic electric and magnetic fields that distort and deflect the electrons beam, preferentially in the direction of the laser polarization[54, 55]. In practice, in a UED experiment, this results in a small fraction of the transmitted electron beam leaking out of the beam stop and adding additional counts. The detector counts at low-s due to plasma deflection show a strong anisotropy due to the polarization dependence of the deflection, while the diffraction pattern is isotropic. We used a Legendre projection of the 2D diffraction patterns to remove anisotropic contributions and keep only the isotropic part of the intensity. With this method we were able to remove the plasma-deflected electrons and retrieve the diffraction signal at low scattering angles.

Figure 7 shows a comparison of the experimental ΔsM with the *ab-initio* scattering calculations (Figure 7 (a)) and with the IAM (Figure 7(b)). The same fitting procedure (described in detail in the supplementary material S2) was used in both cases. The fit shown in Figure 7(a) corresponds to the fragment yields given in Table 5. Figures 7(c-d) show the difference between the data and best fit. There is a clear upward trend in the ΔsM at small angles that is accurately captured by the *ab-initio* calculations, but completely missed by the IAM. This increase in signal at low s is due to the net charge of the molecules. There is also a significant discrepancy in the signal at larger s when using the IAM, in part because the fit cannot accurately capture the low-s signal. The residuals show that the *ab-initio* fit is very accurate. The signal-to-noise ratio in the measurement decreases for larger s because the I_{mol} intensity is proportional to s^{-5}. However, it is clear from Figures 7(c-d) that the trend in the residuals is a flat line for the *ab-initio* calculations but contains significant modulations for the IAM that are larger than the statistical variations in the data.

12

6. Conclusion

We have presented a multimodal study of the strong-field induced ionization, fragmentation and isomerization of toluene using momentum-resolved TOF-MS, UED, high-level structure calculations, and *ab-initio* scattering theory. The TOF-MS data was used to select the most prominent fragments that were then used to fit calculated diffraction signals from those fragments to the UED data. This allowed us to extract the yield of the fragments and to distinguish between isomers that cannot be separated in the TOF-MS data. We have also analyzed in detail the comparison between the TOF-MS and UED data. The major considerations are that TOF-MS is only sensitive to charged fragments, while the UED signal is an average over all neutral and charged molecules. We were able to compare the two datasets by distinguishing the products from single and double ionization in the mass spectra, and found consistent results between the two methods. We have also demonstrated that UED from ions can be accurately modeled using *ab initio* scattering methods, provided the electrons deflected from the plasma are removed during the data analysis. This work presents a roadmap for further UED experiments from ions and towards multimodal studies combining TOF-MS, UED, and theory. The methods demonstrated here, combined with femtosecond resolution UED[21, 22, 26] and finer sampling in time, can be applied to reveal not only the ionization products but also the structural dynamics that leads to fragmentation, extending the applicability of femtosecond UED to probe dynamics not only in neutrals but also in ions. Future studies will cover the timescale between 100 fs and hundreds of picosecond, covering both the structural rearrangements leading to fragmentation on the femtosecond scale and the evolving structures over a longer time scale.

Conflict of interest

There are no conflicts of interest to declare.

Author Contributions

Y.X., S.K.S., K.J.W., J.P.F.N. and M.C. planned the UED experiment. Y.X., S.K.S., K.J.W., K.B., S.P., W.D., X.X. carried out the UED experiment. Y.X. analyzed the UED data supervised by M.C. K.B., A.R. and D.R planned the COLTRIMS / TOF experiment, which was carried out by K.B., S.B., K.C., N.M., S.P. and Z.P.. K.B. analyzed the COLTRIMS data under the guidance of A.R. and D.R., with the help from N.M. AMC, LM, HY and PMW carried out the scattering calculations. AMC carried out the structure calculations with assistance from YX and JPFN. YX, KB, MC, AR, DR, AMC and PWW interpreted the data and wrote the manuscript with assistance from all authors.

Acknowledgments

References

1.   Von E.Doering, W. and L.H. Knox, *The Cycloheptatrienylium (Tropylium) Ion.* Journal of the American Chemical Society, 1954. **76**(12): p. 3203-3206.
2.   Lifshitz, C., *Tropylium Ion Formation from Toluene: Solution of an Old Problem in Organic Mass Spectrometry.* Accounts of Chemical Research, 2002. **27**(5): p. 138-144.

3. Jusko, P., et al., *Direct Evidence of the Benzylium and Tropylium Cations as the Two Long-Lived Isomers of C7 H7().* Chemphyschem, 2018.

4. Nguyen, T., M. Aparicio, and M.A. Saleh, *Gas Phase Ionization of Toluene: Benzylium Versus Tropylium Pathway.* Current Physical Chemistry, 2019. **9**(2): p. 138-150.

5. Ausloos, P., *Structure and isomerization of C7H7+ ions formed in the charge-transfer-induced fragmentation of ethylbenzene, toluene, and norbornadiene.* Journal of the American Chemical Society, 1982. **104**(20): p. 5259-5265.

6. Baer, T., et al., *Gas-phase heats of formation of C7H7+ isomers: m-tolyl, p-tolyl, and benzyl ions.* Journal of the American Chemical Society, 1988. **110**(17): p. 5633-5638.

7. Torma, K.G., et al., *Dissociative Photoionization of the C7H8 Isomers Cycloheptatriene and Toluene: Looking at Two Sides of the Same Coin Simultaneously.* J Phys Chem A, 2019. **123**(16): p. 3454-3463.

8. Castillejo, M., et al., *Ionization and fragmentation of aromatic and single-bonded hydrocarbons with 50 fs laser pulses at 800 nm.* Chemical Physics Letters, 1999. **308**(5-6): p. 373-380.

9. Müller, A.M., et al., *Photoionization and photofragmentation of gaseous toluene using 80-fs, 800-nm laser pulses.* The Journal of Chemical Physics, 2000. **112**(21): p. 9289-9300.

10. Müller, A.M., et al., *White-Light-Induced Fragmentation of Toluene.* Physical review letters, 2001. **88**(2): p. 023001.

11. Tang, X.P., et al., *Enhanced fragmentation of toluene through linear and nonlinear increase of the focal spot area of an ultrashort laser pulse.* Physical Review A, 2005. **71**(4): p. 045401.

12. Squire, D.W., M.P. Barbalas, and R.B. Bernstein, *Comparison of multiphoton ionization-fragmentation behavior of benzene, fluorobenzene, and toluene.* The Journal of Physical Chemistry, 1983. **87**(10): p. 1701-1707.

13. Ablikim, U., et al., *Identification of absolute geometries of cis and trans molecular isomers by Coulomb Explosion Imaging.* Scientific Reports, 2016. **6**(1): p. 38202.

14. Bürgi, H.B., *Stereochemical Applications of Gas-Phase Electron Diffraction. Edited by I. Hargittai and M. Hargittai. VCH Verlagsgesellschaft, Weinheim/VCH Publishers, New York 1988. Part A: The Electron Diffraction Technique. XVIII, 563 S., geb. DM 210.00. – ISBN 3-527-26691-7/0-89573-337-4; Part B: Structural Information for Selected Classes of Compounds. XVIII, 511 S., geb. DM 210.00. – ISBN 3-527-26790-5/0-89573-292-0.* Angewandte Chemie, 1989. **101**(12): p. 1756-1757.

15. Shlykov, S.A., et al., *Structure and conformational behavior of N-phenylpiperidine studied by gas-phase electron diffraction and quantum chemical calculations.* Journal of Molecular Structure, 2017. **1132**: p. 3-10.

16. Shlykov, S.A., T.D. Phien, and P.M. Weber, *Intramolecular inversions, structure and conformational behavior of gaseous and liquid N-cyanopiperidine. Comparison with other 1-cyanoheterocyclohexanes.* Journal of Molecular Structure, 2017. **1138**: p. 41-49.

17. Dudek, R.C. and P.M. Weber, *Ultrafast Diffraction Imaging of the Electrocyclic Ring-Opening Reaction of 1,3-Cyclohexadiene.* The Journal of Physical Chemistry A, 2001. **105**(17): p. 4167-4171.

18. Ihee, H., et al., *Direct Imaging of Transient Molecular Structures with Ultrafast Diffraction.* Science, 2001. **291**(5503): p. 458-462.

19. Yang, J., et al., *Imaging of alignment and structural changes of carbon disulfide molecules using ultrafast electron diffraction.* Nature Communications, 2015. **6**: p. 8172.

20. Yang, J., et al., *Diffractive Imaging of Coherent Nuclear Motion in Isolated Molecules.* Physical Review Letters, 2016. **117**(15): p. 153002.

21. Yang, J., et al., *Imaging CF_3I conical intersection and photodissociation dynamics with ultrafast electron diffraction.* Science, 2018. **361**(6397): p. 64.

22. Wilkin, K.J., et al., *Diffractive imaging of dissociation and ground-state dynamics in a complex molecule.* Physical Review A, 2019. **100**(2): p. 023402.

23.   Wolf, T.J.A., et al., *The photochemical ring-opening of 1,3-cyclohexadiene imaged by ultrafast electron diffraction.* Nature Chemistry, 2019.

24.   Ischenko, A.A., P.M. Weber, and R.J.D. Miller, *Capturing Chemistry in Action with Electrons: Realization of Atomically Resolved Reaction Dynamics.* Chemical Reviews, 2017. **117**(16): p. 11066-11124.

25.   Ischenko, A.A., P.M. Weber, and R.J. Dwayne Miller, *Transient structures and chemical reaction dynamics.* Russian Chemical Reviews, 2017. **86**(12): p. 1173-1253.

26.   Xiong, Y., K.J. Wilkin, and M. Centurion, *High-resolution movies of molecular rotational dynamics captured with ultrafast electron diffraction.* Physical Review Research, 2020. **2**(4): p. 043064.

27.   Lechtken, A., et al., *Structure determination of gold clusters by trapped ion electron diffraction: Au(14)(-)-Au(19)(-).* Phys Chem Chem Phys, 2009. **11**(21): p. 4344-50.

28.   Schooss, D., et al., *The structures of Ag55+ and Ag55- : trapped ion electron diffraction and density functional theory.* Nano Lett, 2005. **5**(10): p. 1972-7.

29.   Maier-Borst, M., et al., *Electron diffraction of trapped cluster ions.* Physical Review A, 1999. **59**(5): p. R3162-R3165.

30.   Soeda, T., et al., *Quantitative electron diffraction study of cation configuration and irradiation induced displacement in magnesium aluminate spinel crystals.* Journal of Electron Microscopy, 1999. **48**(5): p. 531-536.

31.   Yang, J., et al., *Femtosecond gas phase electron diffraction with MeV electrons.* Faraday Discussions, 2016. **194**(0): p. 563-581.

32.   Shibata, S., et al., *Chemical bonding effect in electron scattering by gaseous molecules.* Journal of Molecular Structure, 2002. **641**(1): p. 1-6.

33.   Zandi, O., et al., *High current table-top setup for femtosecond gas electron diffraction.* Structural Dynamics, 2017. **4**(4): p. 044022.

34.   Xiong, Y., K.J. Wilkin, and M. Centurion, *High-resolution movies of molecular rotational dynamics captured with ultrafast electron diffraction.* Physical Review Research, 2020. **2**(4).

35.   Otto, M.R., et al., *Solving the Jitter Problem in Microwave Compressed Ultrafast Electron Diffraction Instruments: Robust Sub-50 fs Cavity-Laser Phase Stabilization.* 2017.

36.   Zandi, O., K.J. Wilkin, and M. Centurion, *Implementation and modeling of a femtosecond laser-activated streak camera.* Review of Scientific Instruments, 2017. **88**(6): p. 063305.

37.   Charles Williamson, J. and A.H. Zewail, *Ultrafast electron diffraction. Velocity mismatch and temporal resolution in crossed-beam experiments.* Chemical Physics Letters, 1993. **209**(1): p. 10-16.

38.   Malakar, Y., et al., *Time-resolved imaging of bound and dissociating nuclear wave packets in strong-field ionized iodomethane.* Physical Chemistry Chemical Physics, 2019. **21**(26): p. 14090-14102.

39.   Rudenko, A., et al., *Resonant structures in the low-energy electron continuum for single ionization of atoms in the tunnelling regime.* Journal of Physics B: Atomic, Molecular and Optical Physics, 2004. **37**(24): p. L407-L413.

40.   Jesus, V.L.B.d., et al., *Atomic structure dependence of nonsequential double ionization of He, Ne and Ar in strong laser pulses.* Journal of Physics B: Atomic, Molecular and Optical Physics, 2004. **37**(8): p. L161-L167.

41.   Ullrich, J., et al., *Recoil-ion and electron momentum spectroscopy: reaction-microscopes.* Reports on Progress in Physics, 2003. **66**(9): p. 1463-1545.

42.   Ullrich, J., et al., *Recoil-ion momentum spectroscopy.* Journal of Physics B: Atomic, Molecular and Optical Physics, 1997. **30**(13): p. 2917-2974.

43.   Straub, H.C., et al., *Absolute detection efficiency of a microchannel plate detector for kilo-electron volt energy ions.* Review of Scientific Instruments, 1999. **70**(11): p. 4238-4240.

44.   Ihee, H., et al., *Ultrafast Electron Diffraction and Structural Dynamics: Transient Intermediates in the Elimination Reaction of C2F4I2.* The Journal of Physical Chemistry A, 2002. **106**(16): p. 4087-4103.

45.   Zotev, N., et al., *Excited Electronic States in Total Isotropic Scattering from Molecules.* J Chem Theory Comput, 2020. **16**(4): p. 2594-2605.

46.   Wang, J. and V.H. Smith, *Evaluation of cross sections for X-ray and high-energy electron scattering from molecular systems.* International Journal of Quantum Chemistry, 1994. **52**(5): p. 1145-1151.

47.   Northey, T., et al., *Elastic X-ray scattering from state-selected molecules.* J Chem Phys, 2016. **145**(15): p. 154304.

48.   Werner, H.-J., et al., *Molpro: a general-purpose quantum chemistry program package.* Wiley Interdisciplinary Reviews: Computational Molecular Science, 2012. **2**(2): p. 242-253.

49.   Stankus, B., et al., *Ultrafast X-ray scattering reveals vibrational coherence following Rydberg excitation.* Nature Chemistry, 2019. **11**(8): p. 716-721.

50.   Yong, H., et al., *Observation of the molecular response to light upon photoexcitation.* Nature Communications, 2020. **11**(1): p. 2157.

51.   Haiwang Yong, A.M.C., Lingyu Ma, Brian Stankus, Michael P. Minitti, Adam Kirrander, Peter M. Weber,, *Determination of Excited State Molecular Structures from Time-Resolved Gas-Phase X-Ray Scattering.* Faraday Discussions (submitted).

52.   Yong, H., et al., *Scattering off molecules far from equilibrium.* The Journal of Chemical Physics, 2019. **151**(8): p. 084301.

53.   Yang, J., et al., *Simultaneous observation of nuclear and electronic dynamics by ultrafast electron diffraction.* Science, 2020. **368**(6493): p. 885.

54.   Centurion, M., et al., *Picosecond electron deflectometry of optical-field ionized plasmas.* Nature Photonics, 2008. **2**(5): p. 315-318.

55.   Centurion, M., et al., *Picosecond imaging of low-density plasmas by electron deflectometry.* Optics Letters, 2009. **34**(4): p. 539-541.
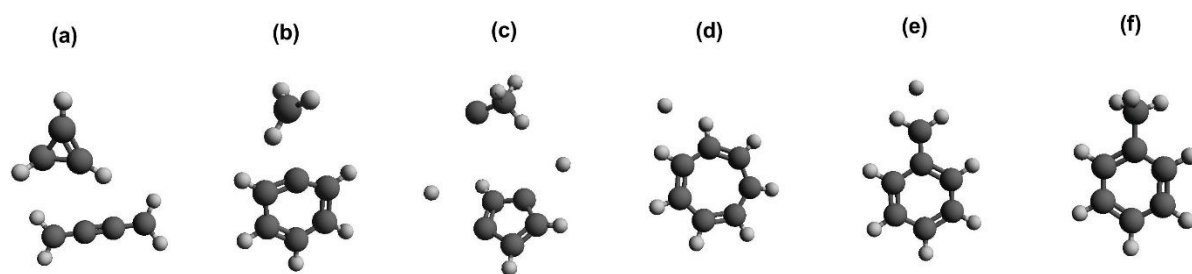
Figure 1. Three-dimensional models of some of the products of toluene ionization. The structures were calculated using the methods described in the text in section 4.2. The fragments are a) $(C_4H_4^+, C_3H_4^+)$, b) $(C_6H_5^+, CH_3^+)$, c) $(C_5H_3+, C_2H_3^+)$, d) tropylium Tr^+, e) benzylum (Bz^+), and f) ionized toluene (Tol^+)
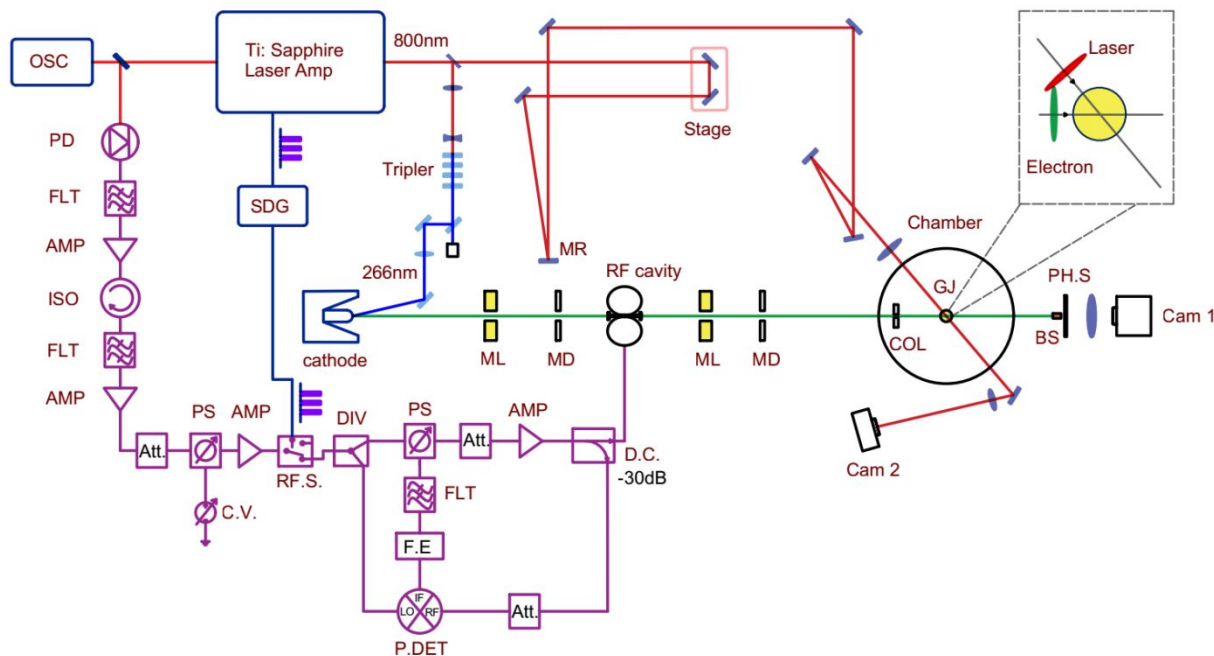
Figure 2. Diagram of the experimental layout for the UED experiment (not to scale). The lines drawn in red color correspond to the path of the 800 nm wavelength laser pulse. A fraction of the laser is converted to the third harmonic at 267 nm to drive the photocathode, with the path shown here in light blue. The path drawn in green corresponds to the electron beam trajectory from the photocathode to the detector. Camera 1 captures the light generated by the electrons impinging on the phosphor screen. Camera 2 is used to monitor the laser pulse. The path in purple corresponds to the 3 GHz RF signal used to drive the RF cavity. The dark blue path is the electric 5 kHz trigger signal from the laser control unit to control the release timing of laser pulse and 3 GHz pulse. The inset shows a sketch of geometry of laser and electron pulse at the interaction region. OSC=oscillator, PD=photo diode, FLT=filter, AMP=amplifier, ISO=isolator, SDG=coherent signal delay generator, Att.=attenuator, RF.S=RF switch, DIV=power divider, PS=phase shifter, C.V.= control voltage, F.E.=feedback electronics, P.DET=phase detector, D.C.=directional coupler, MR=mirror, ML=magnetic lens, MD=magnetic deflector, COL=collimator, GJ=gas jet, BS=beam stop, PH.S=phosphorus screen, Cam=camera.
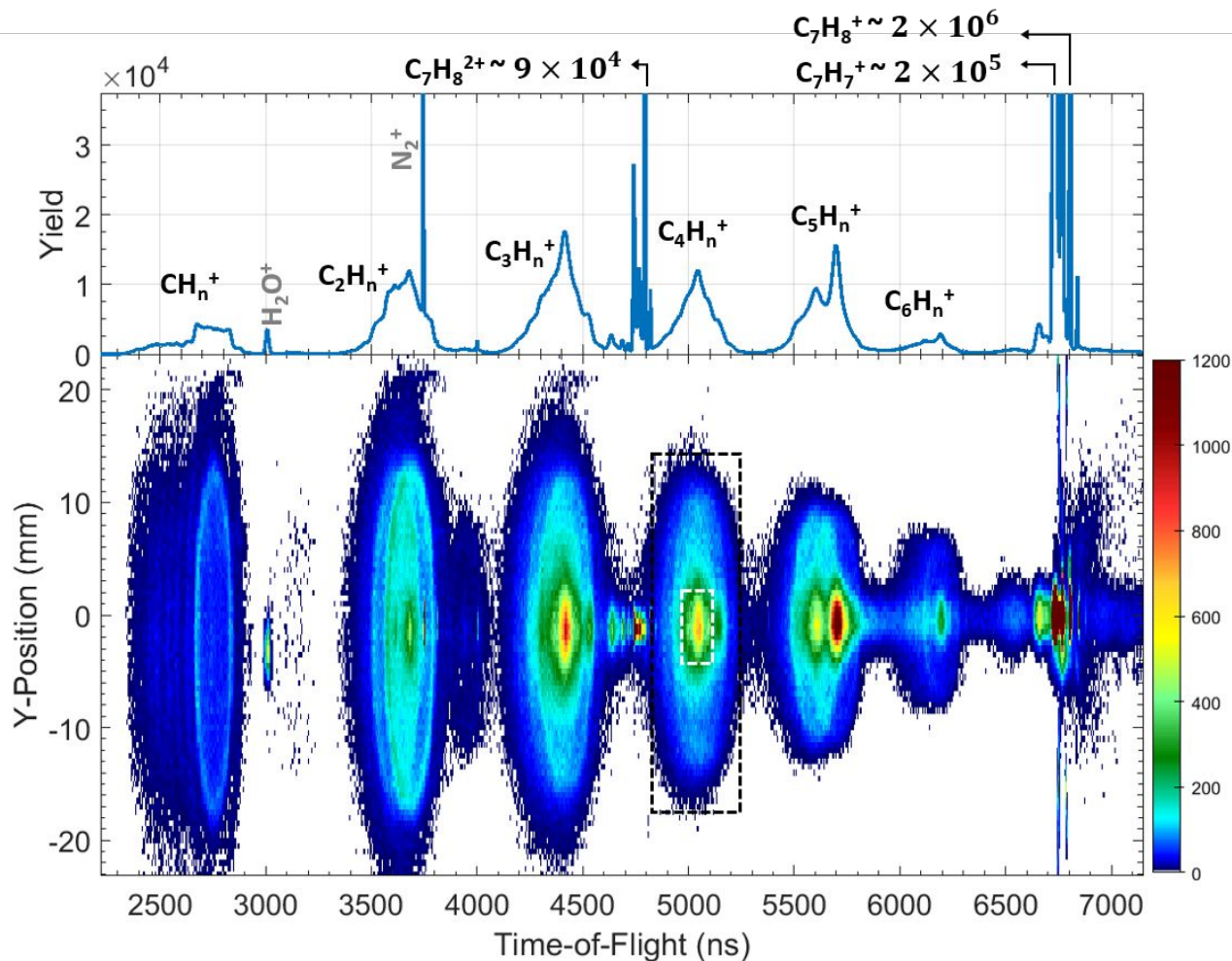
Figure 3. Ion time-of-flight mass spectrum (top) and two-dimensional spectrum of the detector hit position (along the laser propagation direction) plotted as a function of ion time-of-flight (bottom) of toluene after strong-field ionization at 130 TW/cm². The laser polarization is along the time-of-flight axis. Contributions from residual gas are labeled in grey. The peaks corresponding to the parent ion, dication, and the parent ion with one hydrogen loss are cut in order to zoom in on the fragment ions; their peak maxima are indicated above each peak. The white and black dashed rectangles show the regions of interest used to estimate the yield of fragments stemming from single and double ionization, respectively (see text).
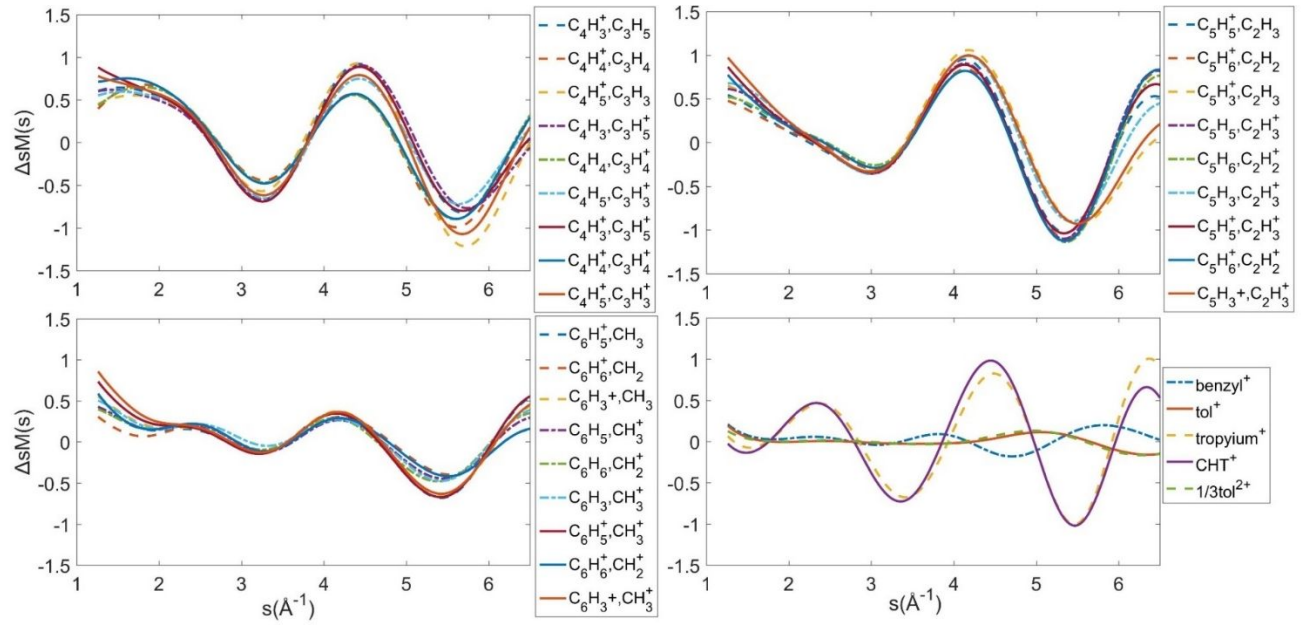
Figure 4. Simulated ΔsM of fragment pairs and other ionic products using *ab initio* computation.
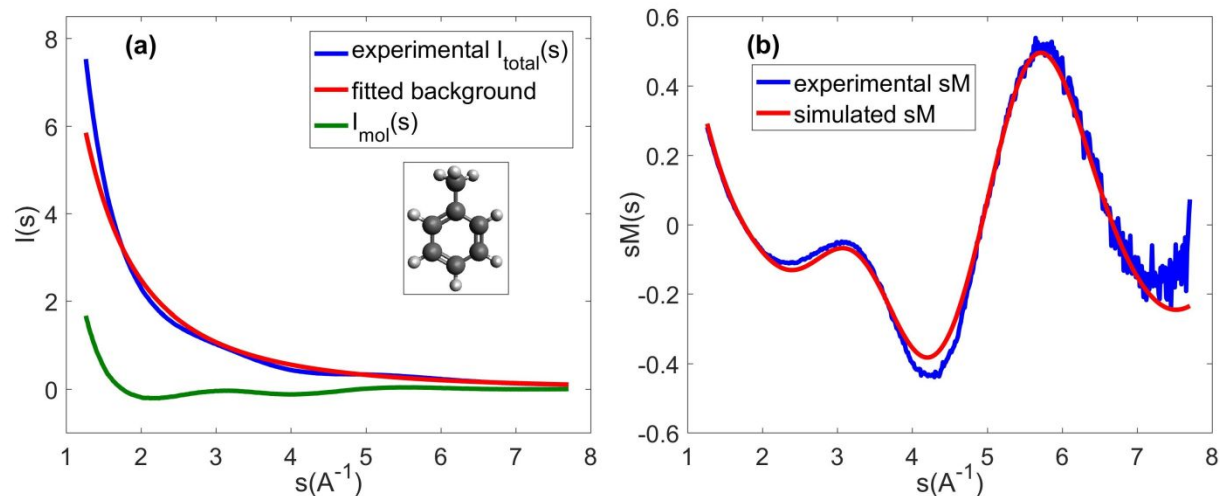
Figure 5. Static diffraction of toluene with a simulation of the diffraction signal based on the IAM. (a) The blue curve shows an azimuthally averaged experimental diffraction pattern after subtraction of the background image measured without gas in the chamber. The red curve shows the fitted background, including the atomic scattering I_{at} and other background scattering. The green curve shows the molecular scattering I_{mol} by taking the difference of I_{mol} and the fitted background. The inset shows the molecular structure of toluene. (b) The simulated (red) and experimental (blue) modified diffraction intensity sM(s) of toluene. The experimental sM is calculated from I_{mol} in (a) and theoretical I_{at}.
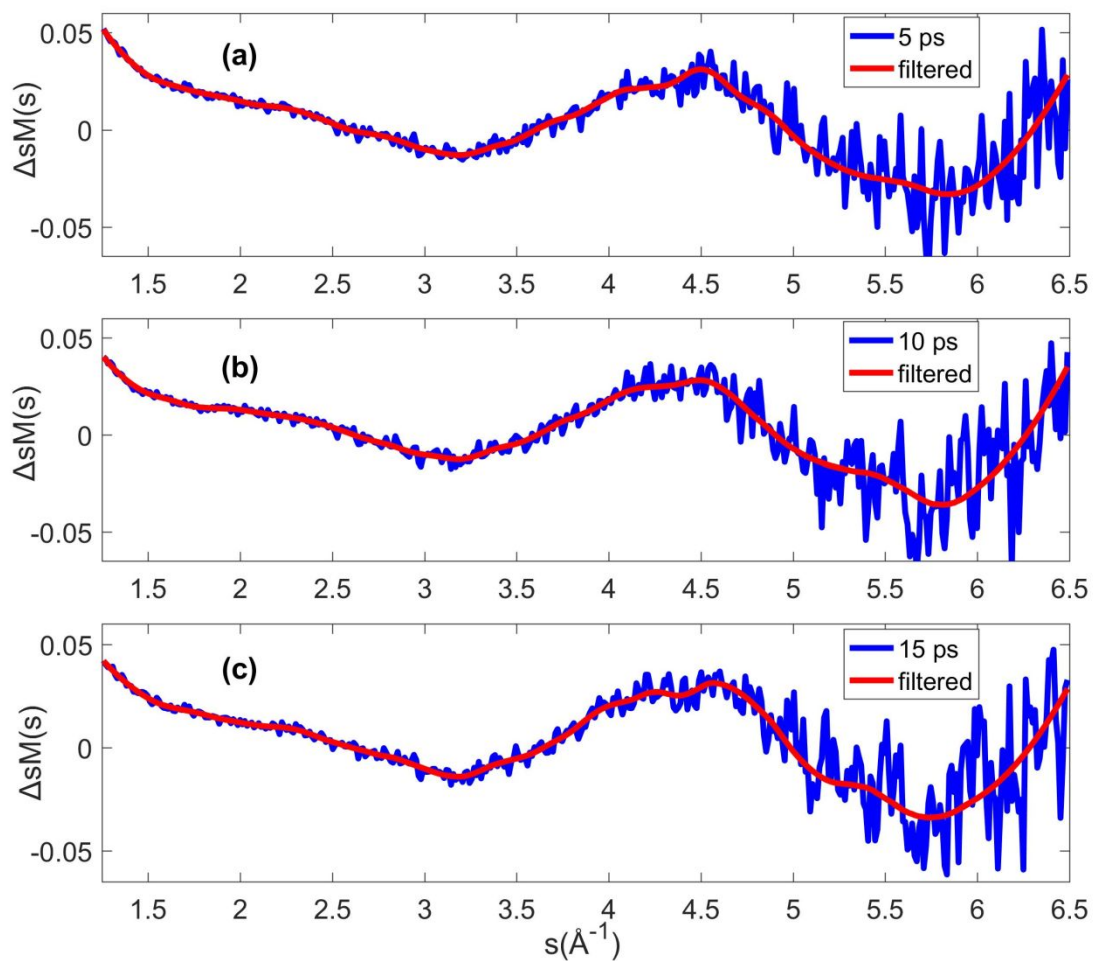
Figure 6. Experimental ΔsM at different times delays (a) 5 ps, (b) 10 ps and (c) 15 ps. The blue lines show the ΔsM while the red lines show the data after a low-pass filter.
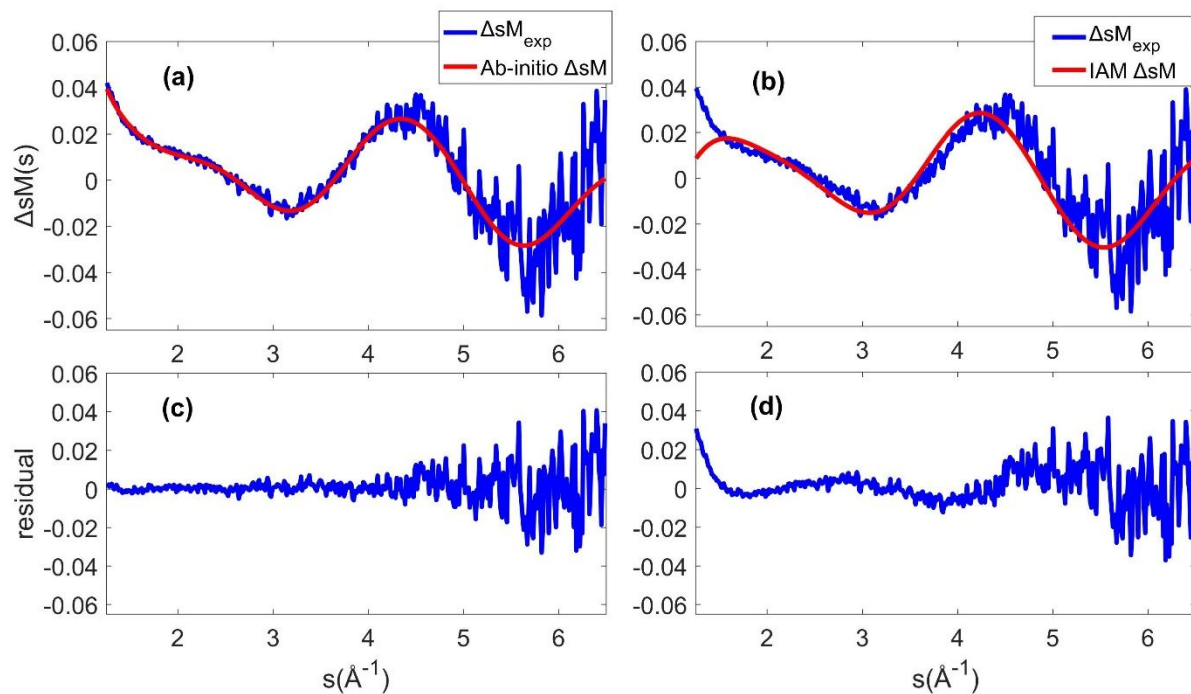
Figure 7. Fitting of the ΔsM from the combined data at 3 time delays after time zero. (a) Fitting with *ab-initio* electron scattering calculation; (b) Fitting with scattering simulation using independent atom model; (c-d) are the residual of the fitting shown in (a-b).

Strong-field induced fragmentation and isomerization of toluene probed by ultrafast femtosecond electron diffraction and mass spectrometry

– Supporting Information–

Yanwei Xiong[1], Kurtis Borne[2], Andrés Moreno Carrascosa[3], Sajib Kumar Saha[1], Kyle J. Wilkin[1], Mengqi Yang[4] ,Surjendu Bhattacharyya[2] , Keyu Chen[2], Wenpeng Du[3], Lingyu Ma[3] , Nathan Marshall[2] , J. Pedro F. Nunes[1], Shashank Pathak[2], Zane Phelps[2], Xuan Xu[3], Haiwang Yong[3], Kenneth Lopata[4], Peter M. Weber[3], Artem Rudenko[2], Daniel Rolles[2], Martin Centurion[1]

[1]University of Nebraska – Lincoln, Lincoln Nebraska, USA

[2]Kansas State University – Manhattan, Kansas, USA

[3]Brown University - Providence, Rhode Island, USA

[4]Louisiana State University, Baton Rouge, Louisiana, USA

S1 Cation yields and laser intensity distribution

Here we describe the differences in the focal geometry of the TOF mass spectrometry and UED experiments, and how that might influence the measurements. The main difference is that the TOF measurement involves a single pulse, the laser, and ions are collected from the whole focal volume. In the UED experiment, the electron beam crosses the laser focus at an angle, thus, only the part of the laser focal volume is sampled by the electron beam. In our case, the electron beam is smaller than the laser beam, so the electrons preferentially sample molecules in the higher intensity region of the laser focus. Assume $P(k, I)$ is the probability of one cation k created from one toluene molecule per laser pulse with an uniform intensity I, and $\rho(I)dI$ is the number of molecules ionized by the laser field over the intensity range dI. The number of cations k generated is $dN(k,I) = P(k,I)\rho(I)dI$. Here $\rho(I)$ is the number density of molecules illuminated by laser intensity I. The molecule number density can be numerically calculated according to the interaction geometry. Integration of the equation over all laser intensities gives the total number of cations k, $N(k) = \int P(k,I)\rho(I)dI$. The relative abundance of cation k is $N(k)/\sum_i N(i)$.
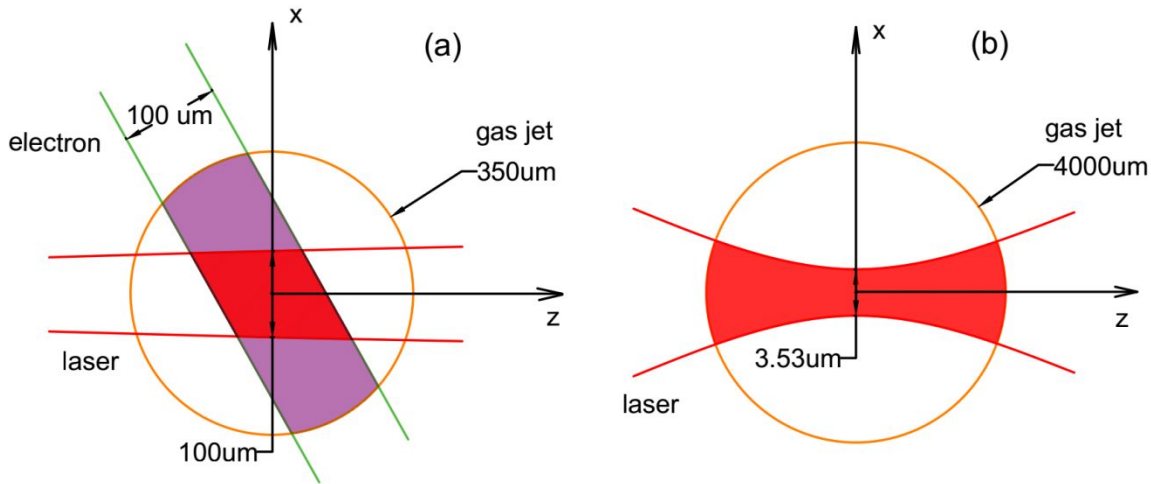
Figure S-1. (a) geometry of laser, electron beam and gas jet in UED experiment; (b) laser and gas jet in TOF

For the UED experiment, the diameter of the beams in the interaction region in full width at half maximum (FWHM) is 350 μm for the gas jet, 100 um×170 μm for the laser beam and 100 μm for the electron beam. In this setup the laser focus (20 μm FWHM) is 5 mm in front of the interaction region. The Rayleigh length is 1.13 mm, and the gas jet is 5 mm away from the laser focus. The laser beam diameter is approximated as constant over the width of the gas jet. The laser intensity in the gas jet can be written as

$$I_{laser\_UED}(x,y) = I_0 e^{-(\frac{x^2}{2c_x^2} + \frac{y^2}{2c_y^2})} \tag{S-1a}$$

The pulse energy E is equal to the integration of $I_{laser\_UED}(x,y)e^{-\frac{t^2}{2c_t^2}}$ over both time and space. Here $I_0 = \frac{E}{(2\pi)^{3/2}c_x c_y c_t} = 116 \text{TW/cm}^2$, based on measurements of pulse duration, energy and spot size. The intensity of the electron beam and gas jet can be written as

$$I_{e\_UED} = \frac{1}{2\pi c_e^2}e^{-\frac{\left(\frac{1}{2}x + \frac{\sqrt{3}}{2}z\right)^2 + y^2}{2c_e^2}} \tag{S-1b}$$

$$I_{gas\_UED} = \frac{1}{2\pi c_g^2}e^{-(\frac{x^2 + z^2}{2c_g^2})} \tag{S-1c}$$

The percentage of molecules that contribute to the diffraction signal and are pumped by a certain laser intensity is determined by the overlap of the electron beam and gas jet. The $1/e^2$ width of the electron beam and gas jet are used to determine the overlap region. The laser intensity range from I_L to I_0 is considered in the numerical calculation, with the assumption that the relative yield of cations generated below laser intensity I_L is negligible. Here we assume I_L=1 TW/cm². The molecule number density $\rho(I)$ is calculated using $\rho(I)= \Delta n/\Delta I$, where Δn is the number of molecules in the spatial region corresponding to laser intensity between I and $I+\Delta I$. The cumulative number of molecules $n(I)$ and density $\rho(I)$ is shown in figure S-2. $n(I)$ represents the number of molecules illuminated by an intensity larger than I.
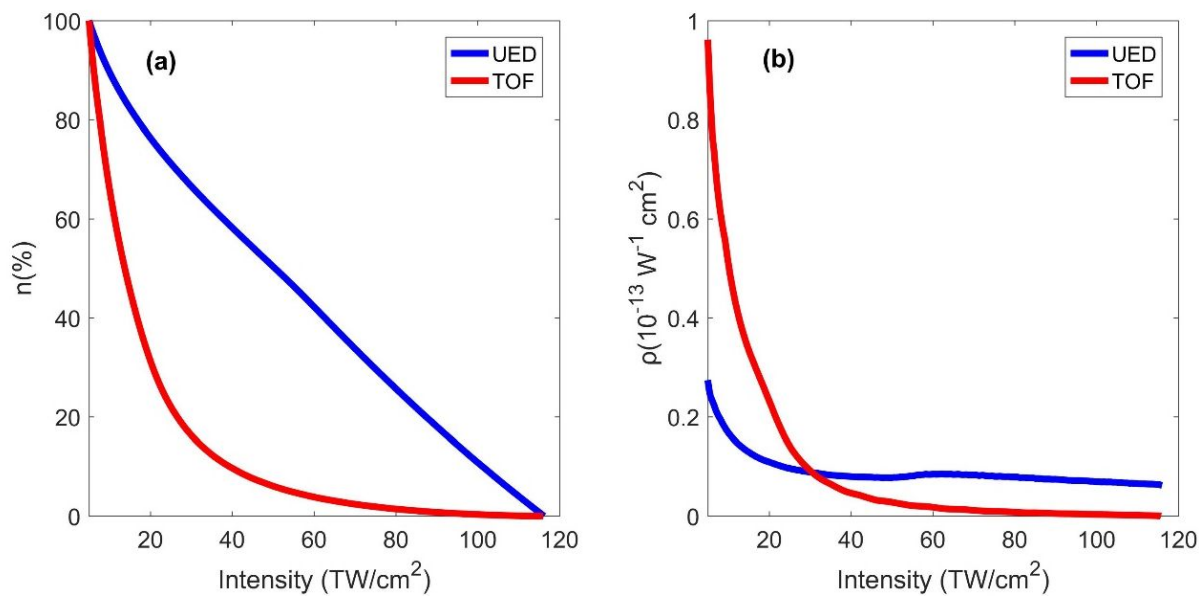
Figure S-2. UED (blue), TOF (red); (a) molecule number cumulative distribution $n(I)$ with total number normalized to 1. (b)the molecule number density $\rho(I) = -dn/dI$

For the TOF mass spectra measurement, the diameter of the gas jet (FWHM) is 4000 μm, the diameter of laser focus (FWHM) 3.53 μm , and Rayleigh length is 10 μm , see figure S-1(b). The laser intensity can be written as

$$I_{laser\_TOF} = I_0\left(\frac{w_0}{w(z)}\right)^2 e^{\frac{-2(x^2+y^2)}{w(z)^2}} \tag{S-2a}$$

where $w(z) = w_0\sqrt{1 + \left(\frac{z}{z_R}\right)^2}$, waist radius w_0=1.5 μm, and Rayleigh length $z_R = \frac{\pi w_0^2}{\lambda}$. The gas jet can be expressed as equation (S-1c) with a different c_g=4000 μm. The $1/e^2$ width of the gas jet and the laser intensity ranging from 1TW/cm² to I_0 are used to calculate the $n(I)$ and $\rho(I)$, shown in figure S-2. The comparison, assuming the same peak intensity in both cases, shows that the UED measurement will sample more molecules at higher intensities, relative to the TOF measurement.

S2 UED data analysis and fitting

Here we describe the steps for processing the UED experimental data.

(a) Image cleanup and normalization: The region of the image blocked by the beam stop is removed from the analysis. Outlier pixels are removed from each image. Each image is normalized to the average value of data within 60×60 pixels around s=2.4A^{-1}.

(b) Difference diffraction signal: The average diffraction pattern of 100 images (each with 1 min. acquisition time) is computed for each of the time delays: -5ps, 5ps, 10ps and 15ps. The diffraction difference pattern are calculated by taking the difference of the combined images for time delays at 5ps, 10ps and 15ps with the reference at -5ps, $\Delta I_{2d}(s,t) = I_{2d}(s,t) - I_{2d}(s,t_{ref} = -5ps)$.

(c) Azimuthal averaging: We applied Legendre projection [1] to the 2-dimensional diffraction difference pattern to obtain the isotropic component, and then azimuthally averaged the 2-dimensional diffraction difference pattern to calculate 1-dimensional diffraction difference signal $\Delta I_{exp}(s,t)$ and corresponding standard errors for each s as $\sigma(s,t)$. The modified diffraction difference intensity is calculated by $\Delta sM_{exp} = \frac{s\Delta I_{exp}}{I_{at\_tol}}$, shown in figure S-3, where I_{at_tol} is the simulated atomic scattering of toluene.
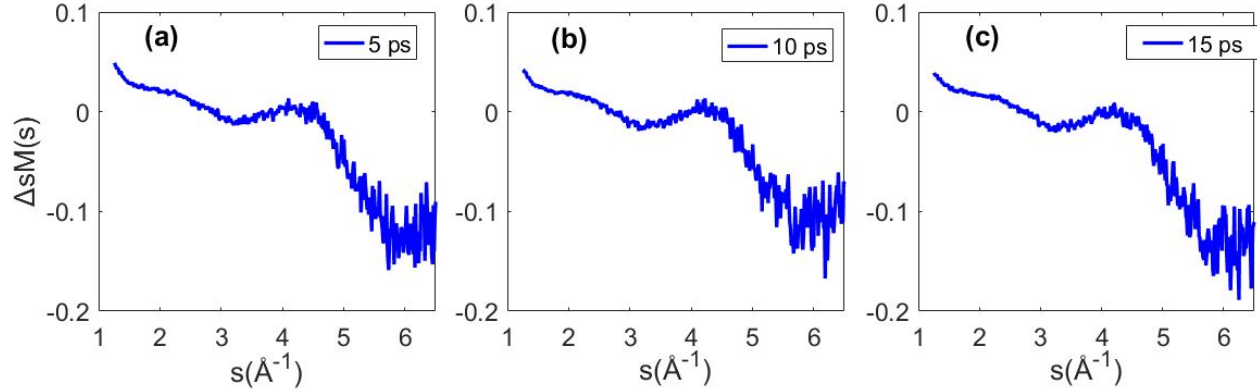
Figure S-3. (a-c) ΔsM_{exp} for different time delays using reference time t_ref=-5ps.

(d) Background correction: The modified diffraction signals have a residual background. To obtain the abundance of fragment pairs from the experimental modified diffraction signal $\Delta sM_{exp}(s)$, we first remove the residual background with the method [2] used to fit the residual background for static diffraction. We construct a function with the simulated ΔsM (labeled as $y_j(s)$ in the following equation) from each fragment pair and a set of parameters, $\Delta sM_T(s,c_j) = \sum_{j=1}^{k} c_j y_j(s)$. The values of experimental data at the zero positions of $\Delta sM_t(s,c_j)$ are used to fit a background $b(s,c_j)$ with a 2nd order polynomial. The set of coefficients c_j with the constraint $\sum_{j=1}^{k} c_j = $ ef (ef indicates the percentage of toluene ionization) that minimizes the equation $\chi^2(c_1,c_2,...,c_k) = \frac{1}{N-k}\sum_{x=1}^{N}(\frac{Y(x) - b(x,c_j) - Y_T(x,c_j)}{\sigma(x)})^2$ gives the yield of each fragment pair.

(e) Fitting: We used an iterative method to find the local minimum of χ^2. Assume the initial coefficients for each component are $(p_1^1,p_2^1,...,p_k^1)$, we construct the scan range for each coefficient c_j by adding and subtracting a small value δ_j, $(p_j^1 - \delta_j, p_j^1, p_j^1 + \delta_j)$. Therefore, there are 3^k sets of coefficients, one of which gives the minimum value of χ^2, for example $(p_1^1,p_2^1 - \delta_2,...,p_k^1 + \delta_k)$, will be used as the new coefficients $(p_1^2,p_2^2,...,p_k^2)$ for the next iteration. Each iteration follows the gradient of the χ^2 and provides a smaller χ^2. The calculation iterates many times until $\chi^2(p_1^m,p_2^m,...,p_k^m)$ is no more than $\chi^2(p_1^{m+1},p_2^{m+1},...,p_k^{m+1})$. The iterations adjust the coefficients automatically to approach a smaller χ^2 each time until the minimum is found.

(f) Fitting results and standard error: Bootstrapping is used to obtain the standard error of the fitted parameters. 100 images are randomly selected out of the 100 images for each time delay to calculate the $\Delta sM_{exp}(s)$, followed by the parameters fitting, to obtain the parameter and confidence interval of each

component. The simulated sM of the most prevalent cations ($C_4H_4^+$,$C_3H_4^+$), ($C_6H_5^+$,CH_3^+), ($C_5H_3^+$,$C_2H_3^+$), Tr^+, Bz^+ and Tol^+, are chosen to do the fitting for the $\Delta sM_{exp}(s)$. Figure S-4 shows the fitted results of the modified diffraction-difference signal ΔsM at time delays of 5 ps, 10 ps and 15 ps. The combined data set, i.e. the average of the 3 different time delays, is fitted to obtain the normalization constant (ef in Table S-1), which corresponds to the percentage of ionized molecules within the interaction volume. The parameters and the confidence intervals using the bootstrapping approach are shown in table S-1. The fragment yields at different time delays are shown in figure S-5. There is some indication that some fragment yields might increase after 5 ps, although further study is needed to reduce the uncertainties to address this point. Overall the fragment yields observed at different times are in agreement within the measurement uncertainties. The results of the fit are comparable when using different fragment pairs form each group to do the fit. The yields obtained from fitting using the second most prevalent cations ($C_4H_3^+$,$C_3H_5^+$), ($C_6H_5^+$,CH_3), ($C_5H_5^+$,$C_2H_3^+$), Tr^+, Bz^+ and Tol^+ cations is shown in figure S-6, which shows similar results. The results are not very sensitive to the number of hydrogen atoms in each fragment.
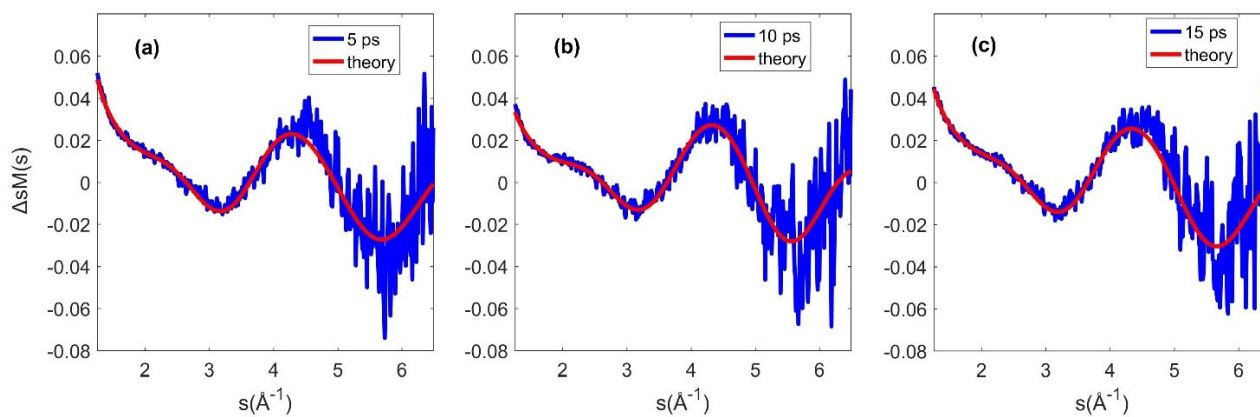
Figure S-4. ΔsM fit for time delay: (a) 5ps, (b)10ps, (c)15ps. experimental ΔsM (blue); theoretical ΔsM (red).
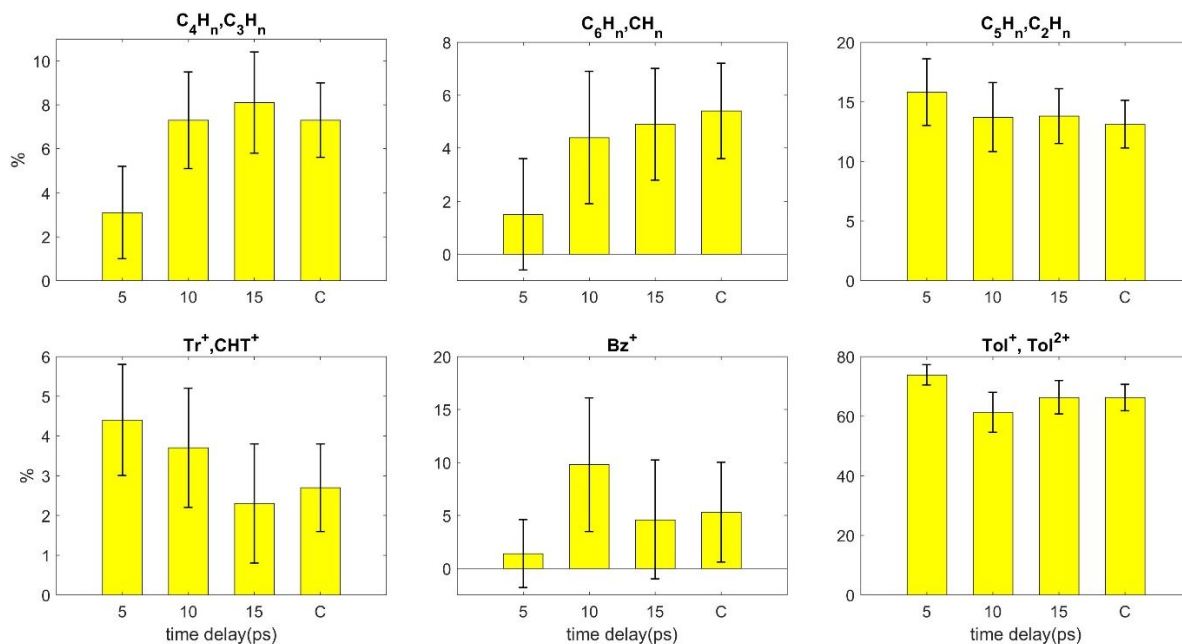
Figure S-5. Cation yields using the fragment pairs ($C_4H_4^+$,$C_3H_4^+$), ($C_6H_5^+$,CH_3^+), ($C_5H_3^+$,$C_2H_3^+$), Tr^+, Bz^+ and Tol^+ cations. The last bar in each plot is the cation yield fitted with combined dataset.

Table S-1. Fitted abundance of the experimental ΔsM. The last row (C) is fitted parameters with the combined data at 3 different time delays after time zero.

%	C_4H_m,C_3H_n	C_6H_m,CH_n	C_5H_m,C_2H_n	Tr^+, CHT^+	Bz^+	Tol^+	ef	χ^2
5ps	3.13±2.14	1.48±2.08	15.77±2.79	4.41±1.41	1.44±3.17	73.78±3.41	0.12	1.88±0.09
10ps	7.26±2.19	4.37±2.51	13.73±2.91	3.70±1.45	9.78±6.34	61.18±6.70	0.12	1.85±0.11
15ps	8.09±2.31	4.95±2.15	13.79±2.34	2.29±1.47	4.63±5.63	66.27±5.58	0.12	1.82±0.09
C	7.30±1.71	5.40±1.82	13.14±2.01	2.66±1.15	5.31±4.68	66.20±4.44	0.12	1.88±0.08
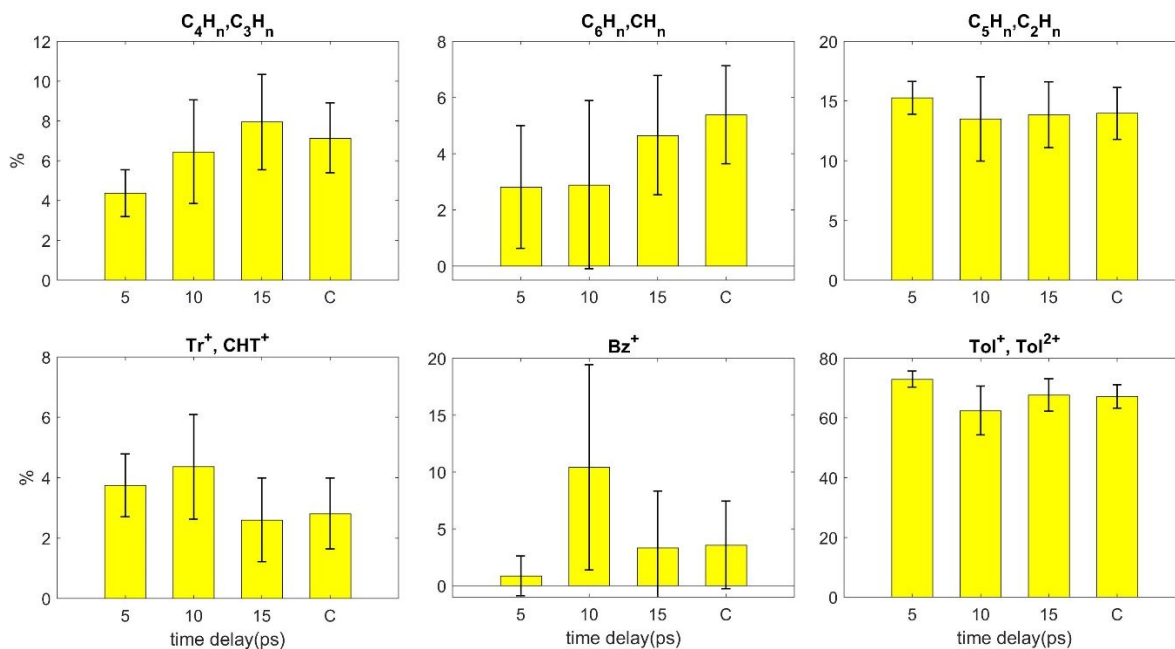
Figure S-6. Cations yields using the fragment pairs $(C_4H_3^+, C_3H_5^+)$, $(C_6H_5^+, CH_3)$, $(C_5H_5^+, C_2H_3^+)$, Tr^+, Bz^+ and Tol^+ cations. The last bar in each plot is the cation yield fitted with combined data at three different time delays after time zero.

S3 Simulated ΔsM using the independent atomic model (IAM)

Here we calculate the ΔsM of the fragment pairs using the IAM for the comparison with the ab-initio scattering calculations (Figure S-7). We use the geometry optimized (section 4.2 main text) with CASSCF level of theory (table 4 in the main text).
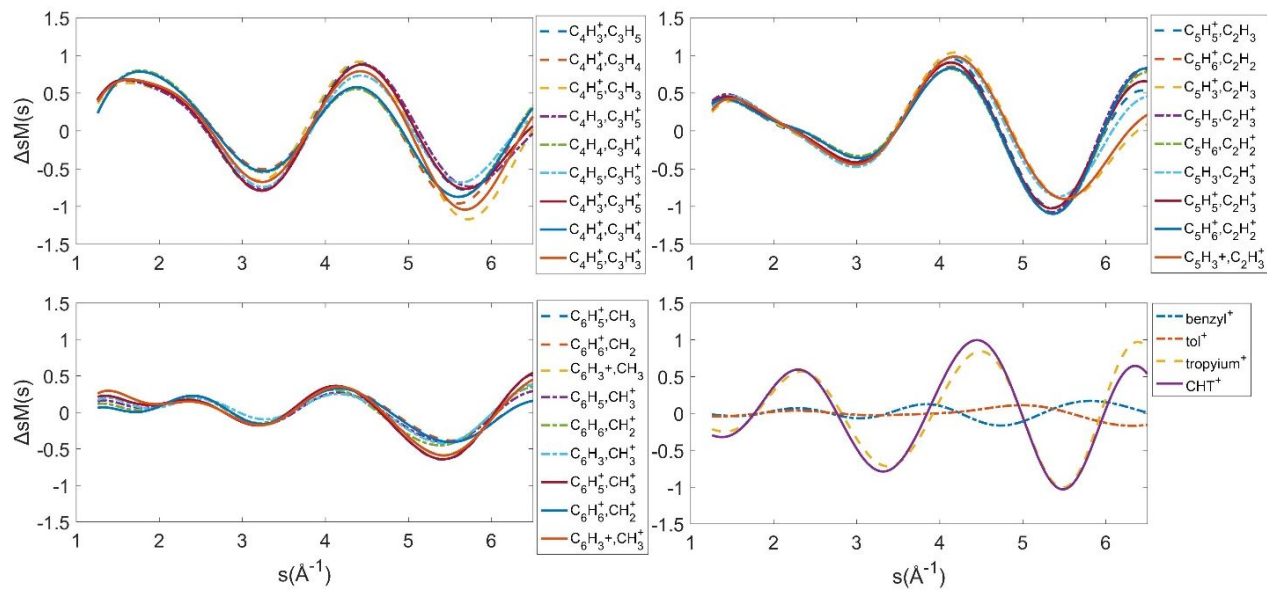
Figure S-7. Simulated ΔsM for fragments pairs using diffraction theory based on the independent atomic model

S-9

Reference

1.   Baskin, J.S. and A.H. Zewail, *Oriented ensembles in ultrafast electron diffraction.* Chemphyschem, 2006. **7**(7): p. 1562-74.

2.   Ihee, H., et al., *Ultrafast Electron Diffraction and Structural Dynamics: Transient Intermediates in the Elimination Reaction of C2F4I2.* The Journal of Physical Chemistry A, 2002. **106**(16): p. 4087-4103.